Title
Microlite orientation in obsidian flow measured by synchrotron X-ray diffraction

Journal
Contributions to Mineralogy and Petrology, 173(7)

ISSN
0010-7999

Authors
Manga, Michael
Voltolini, Marco
Wenk, Hans-Rudolf

Publication Date
2018-07-01

DOI
10.1007/s00410-018-1479-9

Microlite orientation in obsidian flow measured by synchrotron X-ray diffraction

Michael Manga[1], Marco Voltolini[2], Hans-Rudolf Wenk[1]

1 Department of Earth and Planetary Science, University of California, Berkeley, USA

2 Earth and Environmental Sciences Area, Lawrence Berkeley National Laboratory, Berkeley, USA

Abstract

Clinopyroxene and plagioclase (andesine) microlites in an obsidian flow from Glass Mountain (NE California, USA) display strong alignment. Synchrotron X-ray diffraction, coupled with Rietveld analysis, was used to quantify crystallographic-preferred orientation (CPO). Clinopyroxene, with a rod-shaped morphology, shows a strong alignment of [001] in the flow direction and (010) aligned parallel to the inferred flow plane. Andesine, with a platy morphology, displays an alignment of (010) platelets in the flow plane. Some pole densities exceed 90 multiples of random distribution. Applying a model of rigid ellipsoidal inclusions in a viscous matrix, the local pure shear strains are between 2 and 3.

Keywords

Obsidian, Microlite alignment, Texture analysis, Crystal-preferred orientation, Strain estimates

Introduction

Obsidian in natural lava flows preserves a number of textural features that record its eruption and emplacement (e.g., Smith 2002). Structural features range from folds and layering at centimeter-to-decameter scales (Fink 1983; Manley and Fink 1987; Castro and Cashman 1999), to deformed bubbles at the micrometer-to-millimeter scale (e.g., Rust et al. 2003; Gardner et al. 2017) and aligned elongated micrometer-sized crystallites at the smallest scales (Manga 1998; Castro et al. 2002). Together, these textures provide information about flow, fragmentation, and solidification processes.

Microlites are oriented by flow, and their orientation distribution thus offers an opportunity to determine the type of flow and strain experienced by the melt prior to quenching (e.g., Castro et al. 2002; Befus et al. 2014, 2015). Quantitative information, including the relationship between size and orientation, can be obtained with optical microscopy (e.g., Manga 1998; Castro et al. 2004). Because microlites are small, however, it is not usually possible to determine crystallographic orientation, and microlites with diameters smaller than about 1 µm cannot be characterized. Here, we use synchrotron X-ray diffraction and scanning electron microscopy to investigate two rhyolitic obsidian samples from the Glass Mountain lava flow, Medicine Lake Volcano, Northern California.

Synchrotron hard X-ray diffraction proved to be a very useful method for texture analysis in a broad range of different materials from metals (e.g., Wu et al. 2010) to complex clays (e.g., Wenk et al. 2010), slates (e.g., Haerinck et al. 2015), and serpentinite (e.g., Soda and Wenk 2014). This is a first application of the method to volcanic rocks. Contrary to optical microscopy referred to above that describes the shape-preferred orientation (SPO) of particles, X-ray texture analysis provides a quantitative description of the crystallographic orientation distribution of clinopyroxene and plagioclase, averaging over crystallite volumes, not over crystallite numbers. The analysis is by no means trivial in the case of obsidian, since crystallites contribute less than 2% of the volume and diffraction from those crystals is weak compared to scattering from the amorphous glass. Nevertheless, results for SPO and CPO are comparable and can be used to estimate local strain patterns based on Jeffery’s (1922) solution for the motion of rigid ellipsoidal inclusions in a viscous matrix.

Experimental

Samples

The two samples investigated are obsidian fragments from Glass Mountain, CA, USA (41°36′15.5″N/121°28′34.5″W). This ~ 1 km^3 compositionally zoned flow erupted about 1070 AD and is the youngest eruption at the Medicine Lake shield volcano (Grove et al. 1997, Donnelly-Nolan et al. 2016). Optical microscopy reveals a layered structure with layers 2–5 mm in thickness (Fig. 1a). Some layers are more uniform than others. At higher magnification, a strong alignment of needle-shaped microlites is apparent (Fig. 1b). Locally, there is distorted flow around larger inclusions of magnetite (Fig. 1c) and fragments of plagioclase (Fig. 1d).

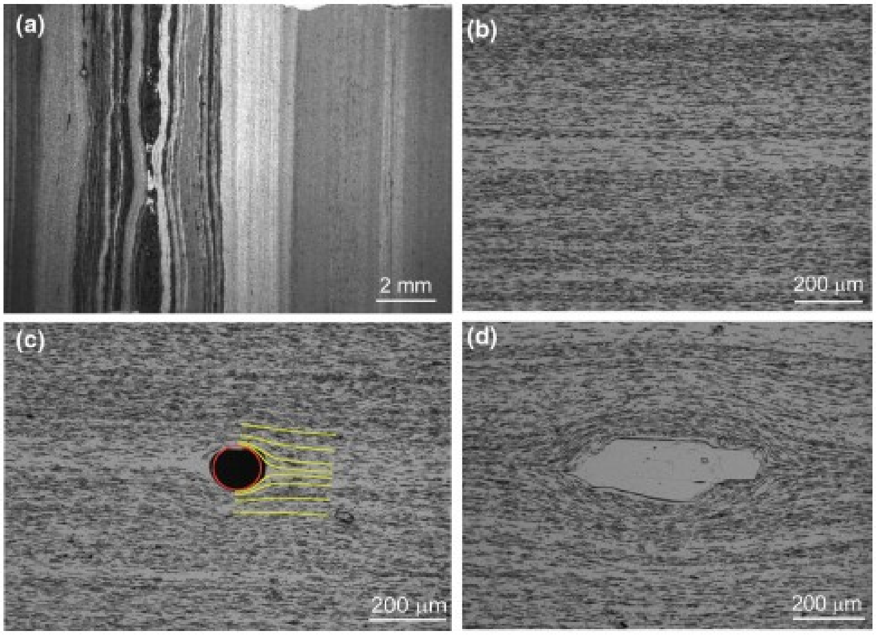

Fig. 1 Optical micrographs of obsidian in sample O1. Plane polarized light. **a** Structure with compositional layering (Os2a), **b** detail of layering with microlites, **c** microlites around an inclusion of magnetite, and **d** inclusion of plagioclase. In **c**, the curves show streamlines for pure shear around a spherical and rigid inclusion

In this study, we focus on homogeneous layers in two samples. In sample 1, microlites are almost exclusively clinopyroxene (Fig. 1b). Sample 2 is a mixture of plagioclase and clinopyroxene microlites. Views of sample 2 with plane polarizers (Fig. 2a, c) and crossed polarizers (Fig. 2b, d), both parallel to the flow direction (Fig. 2a, b) and perpendicular to the flow direction (Fig. 2c, d), show the morphology and the strong alignment of microlites. Clinopyroxenes are needles aligned in the flow direction and plagioclase microlites are platelets aligned in the flow plane. Plagioclase platelets are typically larger in size than clinopyroxene needles which is most obvious with crossed polarizers.

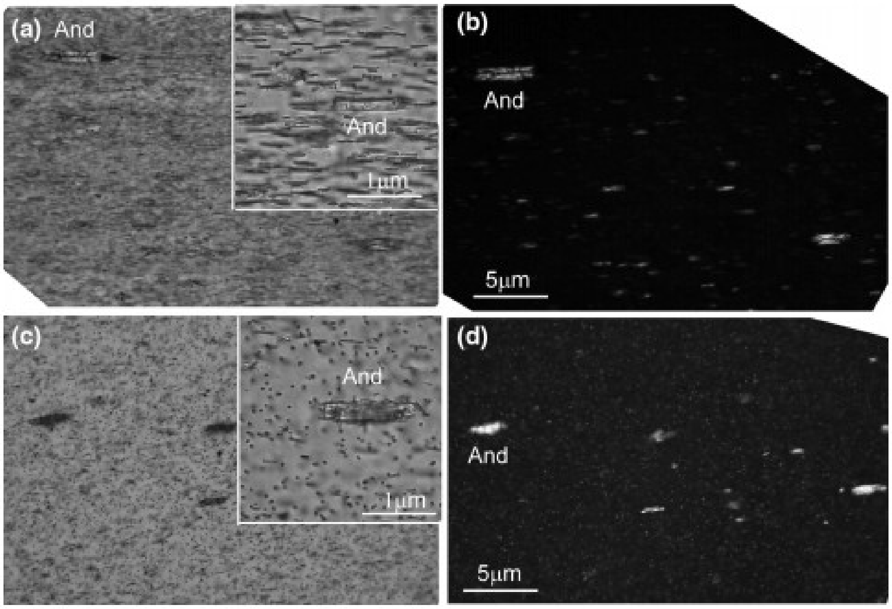

Fig. 2 Optical micrographs of obsidian in sample O2, **a, b** parallel to the flow direction and **c, d** perpendicular to the flow direction; **a, c** are plane polarized light and **b, d** crossed polarizers. Microlites are andesine (And) and clinopyroxene needles (lines in **a** and dots in **c**). In the upper right corner of **a** and **c**, an enlarged segment is displayed

Sample 2 was also analyzed with a JEOL SEM at the Engineering Department of the University of Trento, Italy, to identify the phases and determine their morphology. Back-scattered images, again parallel and perpendicular to the flow direction, are shown in Fig. 3. Pyroxenes are easily recognized, with high contrast. They are prismatic needles with a pseudohexagonal cross section, roughly 2–10 μm long and 0.1–2 μm in diameter. Contrast for plagioclase is weak because of a similar chemical composition as the glass matrix. Some crystals are marked in Fig. 3. They are larger than pyroxenes and have a platelet morphology (see also Fig. 2). They range in size from 2 to 25 μm long to 2–5 μm wide. The chemical compositions of the phases were analyzed with an EDAX EDS system (Fig. 4; Table 1). The pyroxene is identified as ferrous intermediate augite/pigeonite $(Ca_{0.18}, Mg_{0.43}, Fe_{0.36}, Na_{0.03})SiO_3$, plagioclase as calcic andesine $(Ca_{0.40}\ Na_{0.52}\ K_{0.08})(Si_{0.72}, Al_{0.28})O_8$, and glass as high in SiO_2 (> 70%) with significant aluminum, potassium, and sodium.

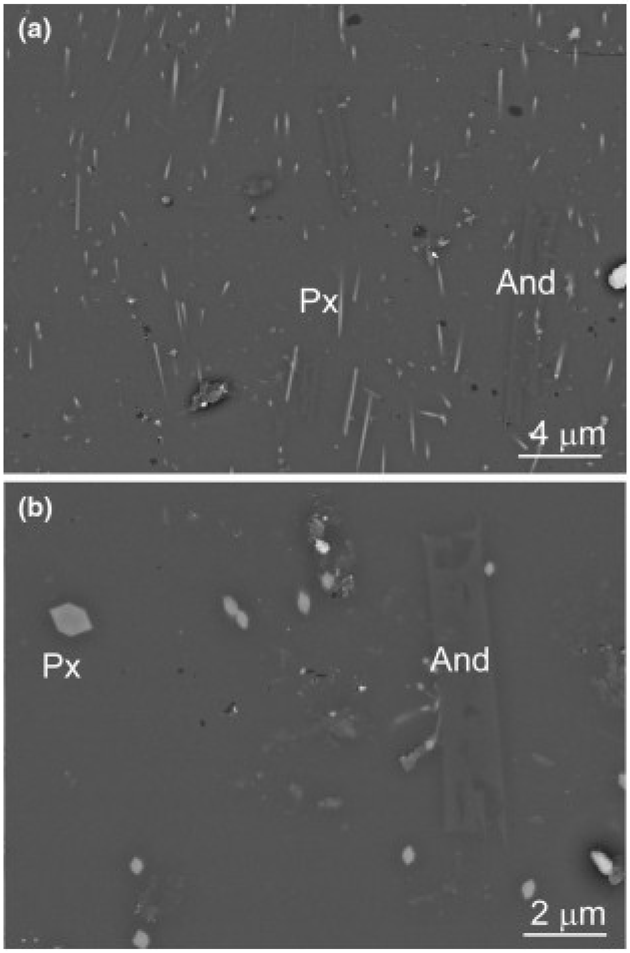

Fig. 3 SEM back-scattered electron images of sample O2, parallel to flow direction (**a**) and perpendicular to flow direction (**b**). The contrast of andesine is very close to that of glass and, therefore, difficult to recognize. The flow plane is vertical

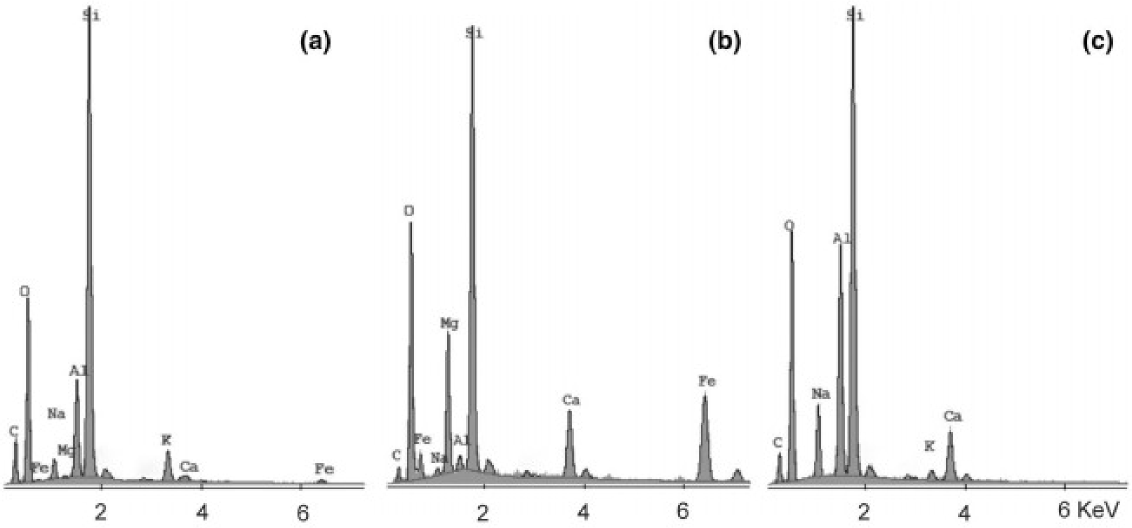

Fig. 4 EDS spectra for **a** glass, **b** clinopyroxene and **c** andesine (compared with Table 2)

Table 1 Chemical composition of glass and microlites in sample 2, measured at two locations with SEM EDS analyses

	Glass		Andesine		Pigeonite	
Na	4.3	4.8	10.0	8.9	1.7	1.2
Mg	0.4	–	–	–	21.0	19.0
Al	14.0	14.5	23.4	23.1	2.1	4.4
Si	72.5	71.5	58.4	58.7	49.3	49.9
K	6.3	6.2	1.4	1.4	0.1	–
Ca	1.1	1.3	6.9	7.9	7.5	10.2
Fe	1.3	1.7	–	–	18.4	15.3

Atomic% (compare with Fig. 4)

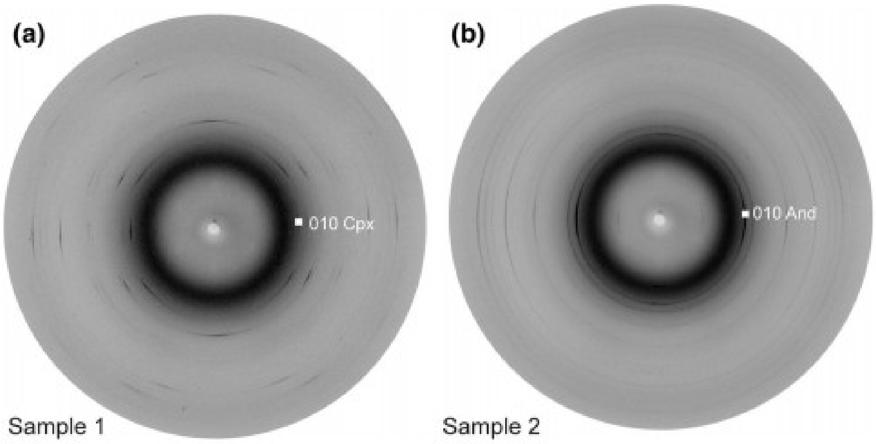

Fig. 5 Selected diffraction images for sample 1 (O11) and sample 2 (O22). Some diffraction peaks are indexed. The broad ring at low angles is due to scattering from silica glass

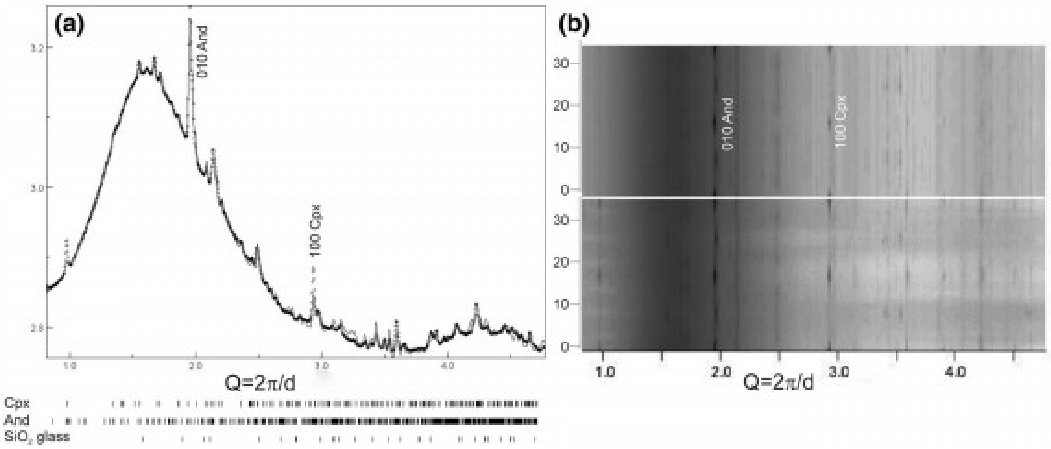

Fig. 6 **a** Azimuthal average of an image for sample O22 with Rietveld fit for clinopyroxene, andesine, and the broad peak for silica glass, approximated by nanocrystalline cristobalite. Dots are observed values and line is the Rietveld fit. Below the spectrum diffraction peaks of the three phases are indicated and some peaks are indexed. **b** Stack of 72 diffraction spectra at 5° azimuthal intervals. Bottom is experimental data and top is Rietveld fit. A logarithmic intensity scale is used to emphasize weak diffractions. Horizontal axis is $Q = 2\pi/d$

Table 2 Volume fractions of glass and microlites based on Rietveld refinement

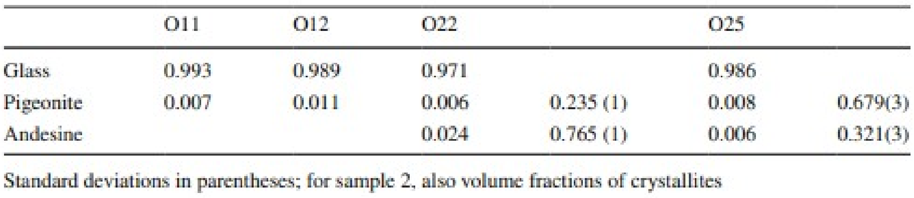

	O11	O12	O22		O25	
Glass	0.993	0.989	0.971		0.986	
Pigeonite	0.007	0.011	0.006	0.235 (1)	0.008	0.679(3)
Andesine			0.024	0.765 (1)	0.006	0.321(3)

Standard deviations in parentheses; for sample 2, also volume fractions of crystallites

Hard X-ray synchrotron diffraction

Samples for the X-ray diffraction experiment were ~ 0.7 mm-thick slabs with the flow plane perpendicular to the slab surface. The diffraction measurements were carried out at beamline 11-ID-C at the Advanced Photon Source (APS) of Argonne National Laboratory. Experiments were performed in transmission geometry. A beam of X-rays ($\lambda = 0.10738$ Å), 0.5 mm in diameter, irradiates the sample, and diffraction patterns were recorded by a Mar345 image plate detector (3450 × 3450 pixels) placed about 2 m behind the sample. Exposure time was 900 s. High energy maximizes sample penetration. The beam size was chosen to give a sufficiently large sample volume (~ 0.2 mm^3) to be representative of a single flow layer. The diffraction images display Debye rings that have intensity variations as a function of the azimuth because of preferred orientation of crystallites (Fig. 5). A dark broad ring is due to scattering from glass and sharp rings are scattering from crystallites.

The sample slab was mounted on a goniometer and was rotated around a horizontal axis perpendicular to the flow plane and the incident X-ray beam. The sample was tilted in 15° increments to seven positions (− 45°, − 30°, − 15°, 0°, 15°, 30°, and 45°) to obtain a good coverage of orientation space for texture analysis. This results in seven diffraction images for each data set.

The flow layers are perpendicular to the tilt axis to avoid overlapping of layers at high tilt angles. For both samples, diffraction images were recorded for two layers (O11, O12, O22, and O25).

Rietveld analysis

The seven diffraction images for each sample location were then analyzed simultaneously with the Rietveld method as implemented in the software MAUD (Lutterotti et al. 2014). Intensities on each diffraction image (Fig. 5) were integrated over 5° azimuthal sectors, resulting in 72 spectra. In the Rietveld method, instrumental parameters, structural and microstructural characteristics, and preferred orientation patterns are refined until an optimal fit is obtained with $7 \times 72 = 504$ diffraction spectra.

First, instrumental parameters such as sample detector distance, detector orientation, and Caglioti parameters defining the diffraction resolution were refined from diffraction data collected for a CeO_2 standard. These instrument parameters were then applied to each of the four obsidian sample data sets.

The Rietveld refinement requires as input the crystallographic characterization of the composing phases. For clinopyroxene, the C2/c structure was used (Clark et al. 1969, # 1000035). For the texture analysis of monoclinic crystals in MAUD, the first setting (*z* monoclinic axis) has to be applied (Matthies and Wenk 2009), but results are shown in the more conventional second setting (*y* monoclinic axis). For plagioclase andesine, $I\bar{1}$ was used which had to be converted to $P\bar{1}$ (Fitzgerald et al. 1986, #9001030). The glass phase, giving rise to the diffuse diffraction peaks at $Q \sim 1.6$ and $4.3\ Å^{-1}$ ($Q = 2\pi/d$), is more difficult to describe. For some refinements, a nanocrystalline form of tetragonal α (low) cristobalite (Hosemann et al. 1991, spacegroup $P4_12_12$) was used, which was first applied to silica glass by Le Bail (1995) and later by Lutterotti et al. (1998).

From seven diffraction images at different tilts for each, polynomial background peaks, phase volume fractions, lattice parameters, grain sizes of phases, and textures (CPO) of clinopyroxene and andesine were refined. Grain sizes (average coherently diffracting domain size) were refined with the isotropic Popa model (Popa 1998), converging for glass at ~ 8 Å which is about the size of the unit cell, for clinopyroxene at ~ 300 Å and for plagioclase at ~ 800 Å.

In a first cycle three phases, glass (modeled as nanocrystalline cristobalite), clinopyroxene, and andesine were included in the refinement to obtain phase proportions, though the assumptions of pure SiO_2 for cristobalite are obviously an approximation. Data and fit for one image of sample O22 are shown for an average spectrum (combining all 72 azimuthal spectra) (Fig. 6a) and for the stack of azimuthal spectra with measured data at the bottom and Rietveld fit on top (Fig. 6b). Note that $Q = 2\pi/d$ is used as horizontal axis, rather than 2θ which depends on the rather arbitrary experiment wavelength, with $2\theta = 2\arcsin(\lambda/2d)$. The large and broad diffraction peak at $Q \sim 1.6$ Å^{-1} (Fig. 6a) is from glass and corresponds to cristobalite (101). Two characteristic peaks of andesine and clinopyroxene are labeled. Volume fractions are summarized in Table 2.

On the “mapplot” (Fig. 6b), a weak azimuthal intensity variation of the strong glass peak at $Q \sim 1.6$ Å^{-1} is present. It was established that this is not due to alignment of disordered silica structure components but an artifact due to the horizontal polarization of the X-ray beam by monochromators. As is obvious from the diffraction images (Fig. 5) and diffraction spectra (Fig. 6) scattering contributions from microlites are weak, because they contribute less than 2% to the sample volume, compared to $>98\%$ from glass and a high general background (Table 2).

In a second cycle of refinements, glass was omitted as a phase, and the contribution of clinopyroxene and andesine microlites was extracted above a “background” modeled with a Gaussian peak to account for the contribution from glass, in addition to a fifth-order polynomial and using a more limited Q range (1.8–4.2 Å^{-1} for sample 1 and 1.4–4.0 Å^{-1} for sample 2). For the texture refinement, the EWIMV method was applied with a resolution of 5° for clinopyroxene and 7.5° for andesine. Rietveld fits for one image of each scan are shown in stacked spectra (Fig. 7). Looking at diffraction peaks in Fig. 6a (bottom), there is a lot of overlap of peaks for these low symmetry minerals and caution is required to have high resolution and avoid artifacts from peak overlaps. The reliability of the fit is expressed in map plots with the good agreement of the fit (Fig. 7 top) with the experimental data (Fig. 7 bottom). These refinements provided the orientation distributions that were exported from MAUD and then used in the software BEARTEX (Wenk et al. 1998) for pole figure calculations. The intensity variations (Figs. 5, 6, 7) are very strong, especially for sample 1 with only clinopyroxene microlites. Average refined lattice parameters are listed in Table 3 and a summary of texture strength is given in Table 4.

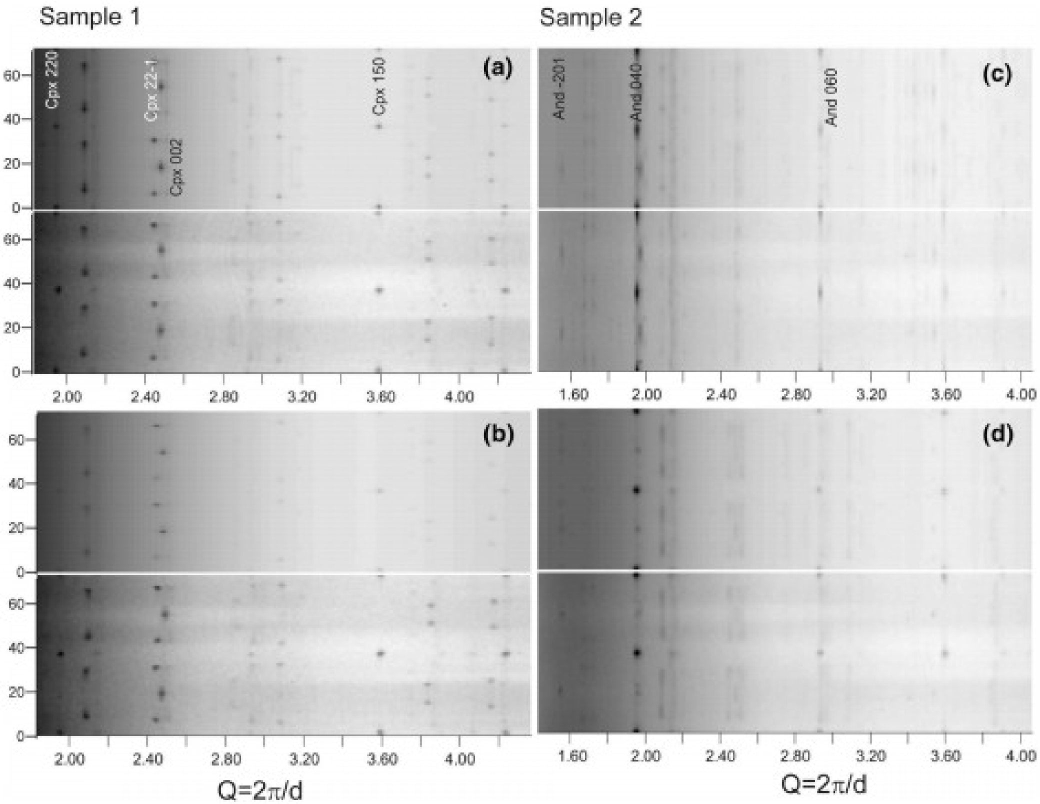

Fig. 7 Refinements of two scans on sample 1 and sample 2. Bottom is stack of 72 experimental spectra for different azimuths (c.f. Fig. 5). Top is corresponding Rietveld fit. **a** O11, **b** O12, **c** O22, and **d** O25. Horizontal scale is $Q=2\pi/d$ (Å^{-1}). Logarithmic intensity scale

Table 3 Average lattice parameters for clinopyroxene and andesine based on Rietveld refinements

	a (Å)	*b* (Å)	*c* (Å)	*α* (°)	*β* (°)	*γ* (°)
Clinopyroxene C2/c (second setting)						
O12	9.7573 (8)	8.8956 (2)	5.2872 (2)		106.810 (6)	
O11	9.7482 (6)	8.8977 (3)	5.2846 (3)		106.782 (5)	
O22	9.7123 (9)	8.9112 (5)	5.3022 (4)		107.177 (8)	
O25	9.7260 (6)	8.8942 (5)	5.2827 (3)		106.894 (6)	
Andesine I-1						
O22	8.1692 (3)	12.8796 (4)	7.1203 (2)	93.280 (4)	116.360 (3)	90.029 (3)
O25	8.1740 (8)	12.9005 (3)	7.1126 (3)	93.149 (11)	115.950 (6)	89.793 (10)

Standard deviations in parentheses

Table 4 Pole figure maxima and minima in multiples of random distribution

	O11		O12		O22		O25		O25-sub
Pigeonite (monoclinic, second setting)									
(100)	13.0	0.2	10.4	0.3	5.8	0.2	7.6	0.5	**13**
(010)	92.6	0.1	58.3	0.3	23.7	0.2	33.3	0.4	**43**
[001]	35.3	0.1	27.5	0.3	12.5	0.3	19.1	0.4	**30**
Andesine									
(100)					4.0	0.4	4.0	0.4	**8**
(010)					19.5	0.4	29.4	0.3	**49**
(001)					3.0	0.4	4.8	0.4	**10**

For sample O25, we also show maxima after subtracting a background of 0.5 ("phon") from pole figures and recalculating ODF (bold)

Results

Optical microscopy provides an overview of the microstructure. The two samples of obsidian are composed of layers, 0.1–2 mm thickness defined by differences in microlite volume fraction, and some layers are more heterogeneous than others (Fig. 1a). Four fairly homogeneous layers were selected for this study (e.g., Figs. 1b, 2). Clinopyroxene microlites are 5–15 µm in length and 0.2–0.5 µm wide (inset in Fig. 2a, c). Many needles have (010) parallel to the inferred flow plane. The needle axis $[001]$ $[\sim(10\bar{2})$ normal] is strongly aligned in the flow direction. Figure 2c, with a view in the flow direction, displays point-like crystallites. SEM images confirm a prismatic morphology with a pseudohexagonal cross section. The prism (010) planes are preferentially aligned in the flow plane (Figs. 3b, 8a).

Fig. 8 Schematic sketch of the morphology of **a** clinopyroxene and **b** andesine crystals. On the right side is an SEM image of a crystallite viewed in the flow direction

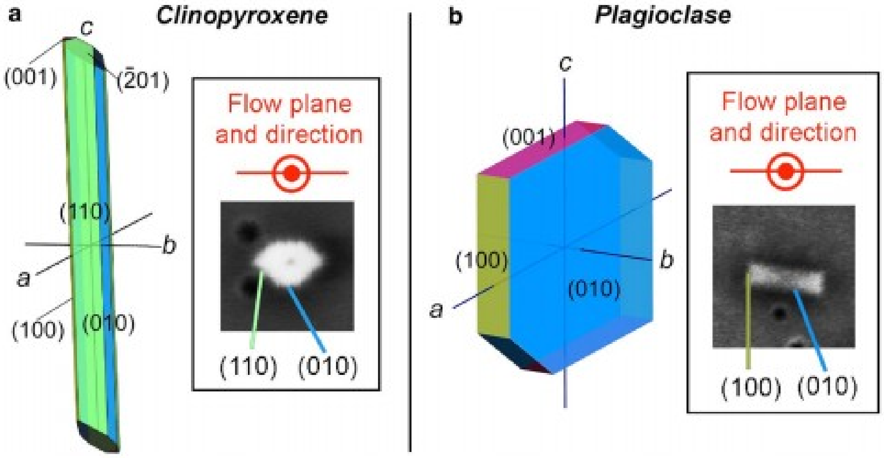

Andesine has a platelet morphology with (010) parallel to the platelet (Figs. 2, 8b). Grains are overall larger than clinopyroxene, 10–100 µm in length and 1–10 µm in width. These platelets are aligned, which is most obvious when viewed with crossed polars where they all shine up simultaneously at a certain rotation (Fig. 2b, d). SEM images display a skeletal morphology of andesine, with some inclusions of clinopyroxene.

The alignment of microlites is consistent with flow of rigid inclusions in a viscous matrix, particularly the disruption of flow around larger inclusions (Fig. 1c, d). Since microlites have this euhedral morphology (Fig. 8), there is a perfect coincidence between shape-preferred orientation (SPO) and crystal-preferred orientation (CPO). The latter is explored with the diffraction experiments.

For the X-ray analysis, we selected layers with intermediate microlite fractions, large enough to provide sufficient diffracting volume and small enough to expect homogeneous flow. Glass volume fractions for O11 and O12 are $> 99\%$. For O22 and O25, there is a slightly larger amount of microlites (~ 0.97 of glass). In O11 and O12, no andesine could be documented. In O22, there is ~ 24% clinopyroxene versus ~ 76% andesine, and in O25, there is ~ 68% clinopyroxene versus ~ 32% andesine (Table 2).

Figures 9, 10 show pole figures for selected crystal directions, after rotating all samples into the same orientation with the flow (layer) plane as projection plane and the flow direction horizontal. The pole figures confirm the qualitative optical results. There is, indeed, very strong preferred orientation in all scans with very high maxima for planes aligned in the flow plane and prism axes aligned in the flow direction as expressed in multiples of a random distribution in Table 3. For pigeonite, the poles to (010) and {110} are aligned preferentially perpendicular to the flow plane, and [001] is parallel to the flow direction (Fig. 9). For andesine, (010) is the platelet plane and aligned in the flow plane (Fig. 10).

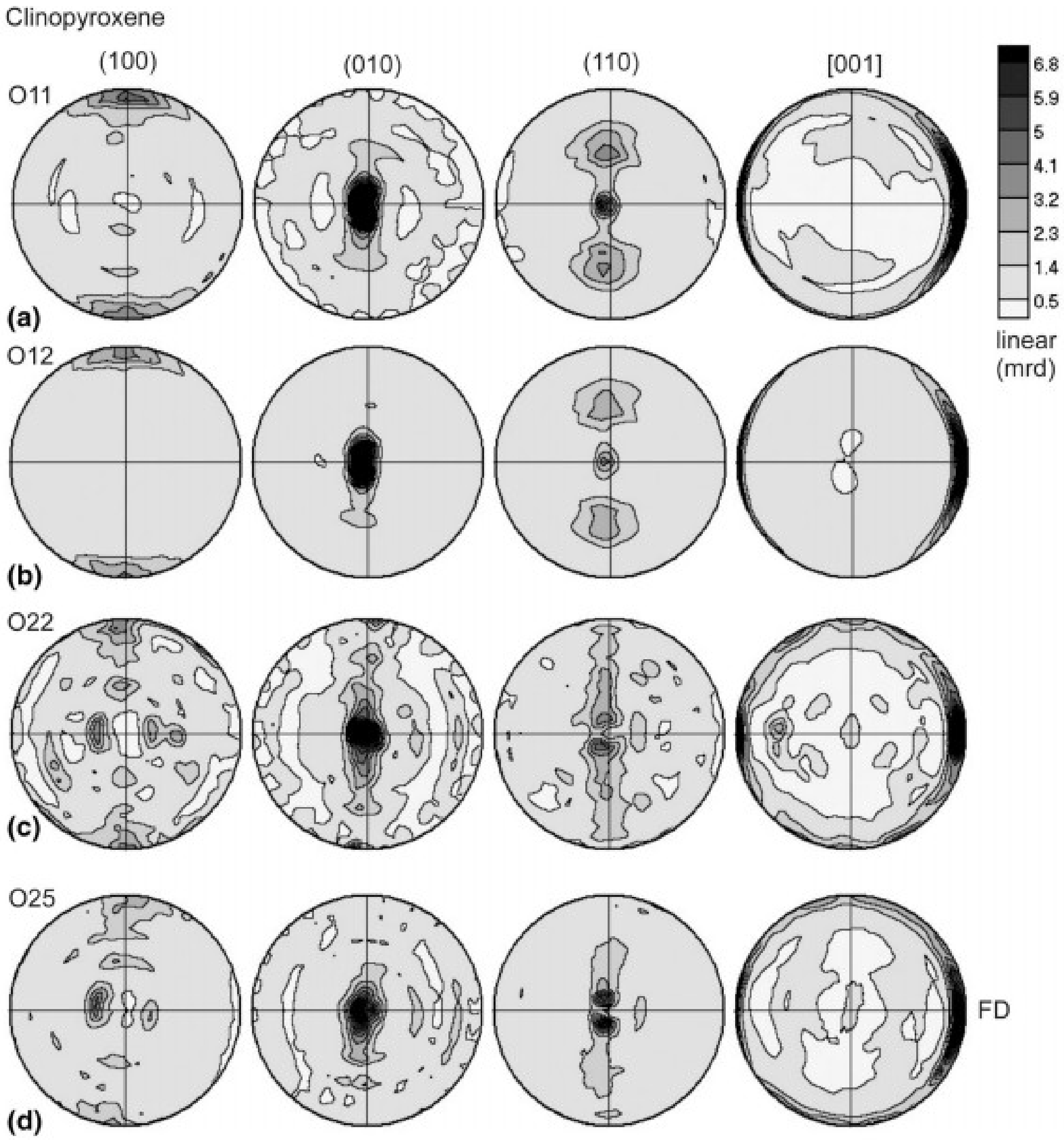

Fig. 9 Pole figures for clinopyroxene for samples 1 and 2 projected on the flow plane. FD is flow direction. Equal area projection, linear pole density scale

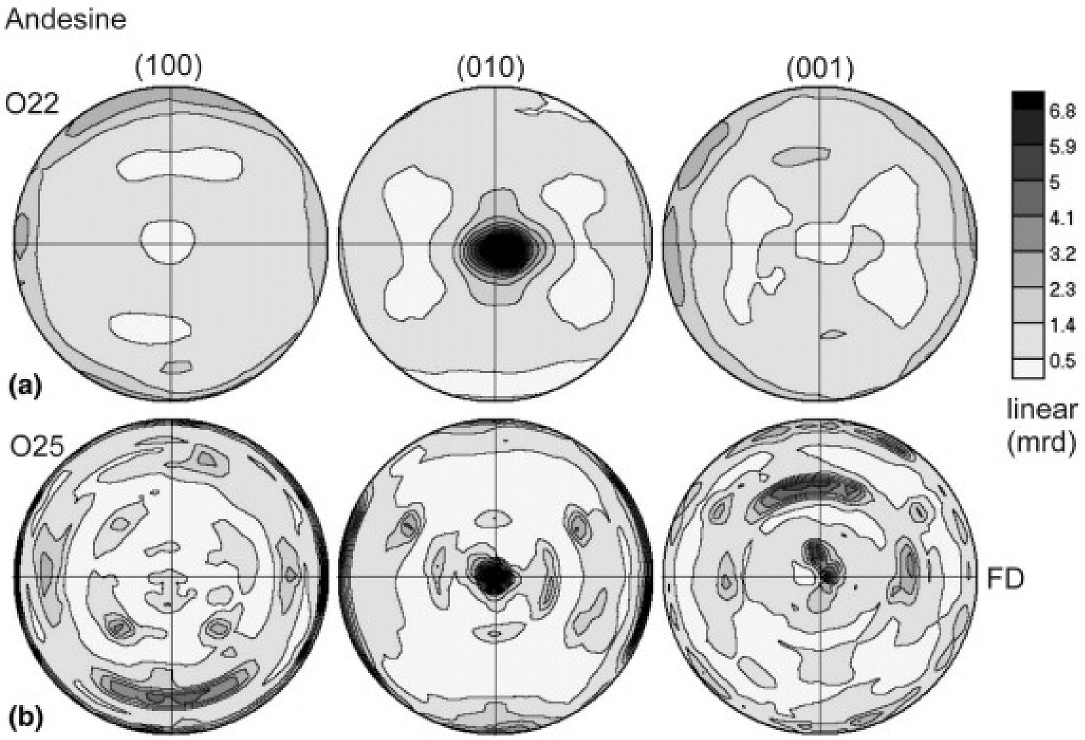

Fig. 10 Pole figures for andesine for sample 2 projected on the flow plane. FD is flow direction. Equal area projection, linear pole density scale

It should be emphasized that the quantitative data analysis is by no means trivial. One issue is the peak overlaps of the low symmetry microlite phases (Fig. 6a). A second problem is the very weak scattering from crystalline microlite phases compared to the broad background of dominant scattering from glass. Most diffraction peaks are less than 10% above background. To minimize problems from overlaps, textures of the two microlite phases were refined separately: first for andesine and then for clinopyroxene. Major overlaps were expected from diffraction on lattice planes aligned parallel to the flow plane and giving a signal at 0 azimuth (bottom of the stack of spectra). Therefore, these spectra were disabled from the refinement, but it turned out that it did not make any difference.

The preferred orientation does not only display very strong peaks (measured in multiples of random distribution, m.r.d.) but also very sharp peaks, especially for clinopyroxene with width of CPO peaks at half maximum ranging from 15° to 25°. All pole figures (Table 4) also show a significant background ranging from 0.1 to 0.5 m.r.d. Part of the background is due to randomly oriented crystallites such as clinopyroxene clusters or dispersion around inclusions (Fig. 1c, d) and nanocrystalline microlites but part may also be an artifact due to the high background and limited counting statistics. Yet, note that in measured diffraction images (Fig. 5) and measured diffraction patterns (bottom of Fig. 7), there is residual intensity for all azimuthal angles, not just for the intensity maxima. For scan O22, we have explored the effect of background and apparent high random contribution by first calculating pole figures, then subtracting from pole figures the random contribution, and then using these new pole figures to calculate new orientation distributions with WIMV in BEARTEX. It turns out that the new orientation maxima have increased by a factor 2–3 (bold numbers in Table 4). These are representative of the aligned crystallites during viscous flow.

Discussion

The alignment of microlites parallel to bands is the result of flow and confirms that the visibly identified layers in obsidian are in fact flow bands. Although the melt may have fractured and rewelded multiple times to create the heterogeneities that define the various layers (e.g., Tuffen et al. 2003; Gonnermann and Manga 2003, 2005; Gardner et al. 2017), the alignment of microlites with the macroscopic layers requires that much of the strain we see accumulated after the last welding event and that microlites were reoriented after the last welding event.

The measurements show that not only are microlites aligned according to their morphology (SPO) in the flow field, but also that their crystallographic axes are aligned (CPO). It is unclear whether the flow-induced orientation has consequences for the crystal habit and their growth during emplacement.

The preferred orientation of microlites in obsidian is an example of alignment of rigid particles in a viscous medium. Flow is governed by Stokes equations for viscous flow, since the Reynolds number is $\ll 1$ owing the high viscosity, $10^{8.6}$ Pa s using the composition in Giachetti et al. (2015), the mean water content of 0.22 weight% reported by Tatlock et al. (1976), a temperature of 850 °C (Waters et al. 2015), and the viscosity model of Giordano et al. (2008). Jeffery (1922) solved the equations for the motion of an ellipsoid at low Reynolds number (Stokes flow). This solution was later advanced by March (1932) to establish the relationship between the orientation of ellipsoidal particles and the overall strain. Sander (1950) applied the March concept to explain preferred orientation of phyllosilicates in slates and there are several applications reviewed by Oertel (1983). If we assume a unit sphere with a random needle distribution and deform the sphere into an ellipsoid with axes $E_1 > E_2, > E_3,$ the particles become aligned, mainly parallel to the principal stretch E_1. According to Oertel (1985):

$$E_1 = {\rho_n}^{1/3},$$

where ρ_n is the pole density of the needles. In addition, from the stretch, we obtain the strain

$$\varepsilon_1 = {\rho_n}^{1/3} - 1.$$

Platelet-shaped particles align with platelet normal preferably parallel to the smallest stretch E_3:

$$E_3 = \rho_p^{-1/3}$$

and strain

$$\varepsilon_3 = \rho_p^{-1/3} - 1.$$

Microlites in obsidian is an ideal case to apply the March model. In the case of O25, we can use the concentration of clinopyroxene [001] in the flow direction to estimate the extensional stretch and strain, and andesine (010) to determine the compressional stretch and strain. With $\rho_n \sim 19$ m.r.d. for clinopyroxene, we obtain $E_1 = 2.7$, i.e., the long ellipsoid axis is 2.7 times longer than the original sphere diameter. This corresponds to a strain $\varepsilon_1 = 1.7$. For andesine platelets with $\rho_p \sim 29$ m.r.d., we obtain a stretch $E_3 = 0.32$ and a strain $\varepsilon_3 = -0.68$.

These values are for the case with a randomly oriented component that is not related to the alignment by flow. For the probably more realistic situation where the random component is subtracted (Table 4, right column, bold), pole density maxima increase greatly. With $\rho_n \sim 30$ m.r.d. for clinopyroxene, we obtain $E_1 = 3.1$, and a strain $\varepsilon_1 = 2.1$, and with $\rho_p \sim 49$ m.r.d. for andesine, we obtain $E_3 = 0.27$, and a strain $\varepsilon_3 = -0.73$.

There is a little evidence for deformation in the intermediate direction, suggesting overall plane strain and pure shear. Further support for the dominance of pure shear is provided by the orientation of the microlites around large inclusions. In Fig. 1c, we also show streamlines (lines parallel to the velocity) for pure shear around a spherical inclusion. As the flow is fully three-dimensional, we show the flow in the mid-plane of the particle and a cross section parallel to the flow direction. Equations for this problem are presented in Manga (2005). The orientations of microlites are very close to the orientation of streamlines for pure shear flow around a rigid inclusion. In contrast, Rust et al. (2003) measured the orientation distribution and aspect ratio of deformed bubbles in a sample from the same flow and inferred that deformation was dominated by simple shear. These two inferences, that there was pure and simple shear, need not be incompatible, since different parts of the flow will experience different strains: pure shear near the top, simple shear near the base (e.g., Buisson and Merle 2002; Ventura 2004). The sample analyzed here was collected from the flow front and about half-way between the surface and the bottom of the flow.

The magnitude of strain is consistent with the previous investigations of microlite orientations and bubble deformation that suggested strains of the order of 2–3 for pure shear (Manga 1998; Castro et al. 2002; Befus et al. 2014, 2015). These estimates all build on the solution of Jeffrey (1922) which is for motion of a single isolated particle. Even though the volume fraction of crystals is small (less than 3%), because the microlites are elongate, there are hydrodynamic interactions between the particles (Rahnama et al. 1995) and these do have a small effect on the orientation distribution for the observed aspect ratios and concentrations in obsidian (Manga 1998).

A number of studies have used optical microscopy to determine the orientation distribution of microlites and then to quantify kinematics: the total strain and flow type that accompanied rhyolite flow emplacement (Castro et al. 2002; Befus et al. 2014, 2015). Such measurements of microlite morphology are very time-consuming and rely on data from individual crystallites. Generally, larger crystallites are selected, because they are optically visible.

The diffraction measurements reported here are based on overall volume fractions. Quantitative texture analysis using hard synchrotron X-rays has advanced through a combination of experiments and data analysis (e.g., Lutterotti et al. 2014; Wenk et al. 2014). A single measurement, e.g., at beamline APS 11-ID-C, takes less than half an hour. Yet, it requires access to a synchrotron which must be obtained through proposals and is usually limited to one or two sessions a year. Data analysis can be very involved depending on sample complexities and it needs some experience.

The CPO patterns are statistical averages over selected sample volumes, and for interpretation of pole figure data, additional information about crystal morphology is required (e.g. Fig. 8). However, the method provides data about multiple minerals and smaller crystals than those resolved with optical methods. It might also allow us to document when different crystal populations nucleated and become oriented, but this would require examining a suite of samples collected at different distances from the vent and at different depths within the flow. The measurements presented here do not provide direct constraints on dynamics (beyond kinematics) and hence emplacement time scales: additional constraints are needed about crystal nucleation and growth rates, or other complementary measurements that constrain time scales.

Diffraction methods provide complementary results compared to optical ones and a combination of the two can be useful. Other methods that could be combined are X-ray or electron nanotomography (e.g., Miao et al. 2016; Midgley et al. 2007; Stampanoni et al. 2010) that have provided information about microstructures in multiphase shales (e.g., Kanitpanyacharoen et al. 2013). Voltolini et al. (2011) used X-ray microtomography to determine shape-preferred orientation of both crystals and vesicles in volcanic rocks and Arzilli et al. (2015) combined tomography with SEM-EBSD to characterize the growth of spherulites from melts. Such examples highlight how diffraction- and imaging-based approaches provide complementary results and might be combined successfully in the future to systematically explore what can be learned from microlites in lava flows.

Conclusions

This study introduces a new method to determine the orientation distribution of microlites in an obsidian flow. With synchrotron X-ray diffraction, we can statistically quantify the orientation of clinopyroxene needles in the flow direction and andesine platelets in the flow plane. Microlites are aligned parallel to layering, confirming that layers are, in fact, flow bands. Based on model of rigid particles in a viscous fluid, we obtain strains 2–3.

Acknowledgements

HRW acknowledges support from NSF (EAR-1343908) and DOE (DE-FG02-05ER15637) and access to beamline 11-ID-C at the Advanced Photon Source (APS) of Argonne National Laboratory. MM is supported by NSF 1724469. We appreciate help from Yang Ren at beamline ID-11 ID-C of APS and Tim Teague for sample preparation. Part of this research was done during a research leave at the University of Trento/Mesiano and HRW is grateful to Luca Lutterotti for the hospitality and guidance in data analysis, and also for access to the SEM and help from Lorena Maines. The authors thank the editor, J. Donnelly-Nolan, and an anonymous reviewer for constructive comments and suggestions. Authors are listed in alphabetical order.

References

Arzilli F, Mancini L, Voltolini M, Cicconi MR, Mohammadi S, Giuli G, Mainprice D, Paris E, Barou F, Carroll MR (2015) Near-liquidus growth of feldspar spherulites in trachytic melts: 3D morphologies and implications in crystallization mechanisms. Lithos 16:93–105

Befus KS, Zinke RW, Jordan JS, Manga M, Gardner JE (2014) Pre-eruptive storage conditions and eruption dynamics of a small rhyolite dome: Douglas Knob, Yellowstone volcanic field, USA. Bull Volcanol 76(3):1–12. https://doi.org/10.1007/s00445-014-0808-8

Befus KS, Manga M, Gardner JE, Williams M (2015) Ascent and emplacement dynamics of obsidian lavas inferred from microlite textures. Bull Volcanol 77(10):88. https://doi.org/10.1007/s00445-015-0971-6

Buisson C, Merle O (2002) Experiments on internal strain in lava dome cross sections. Bull Volcanol 64(6):363–371. https://doi.org/10.1007/s00445-002-0213-6

Castro J, Cashman KV (1999) Constraints on rheology of obsidian lavas based on mesoscopic folds. J Struct Geol 21(7):807–819. https://doi.org/10.1016/S0191-8141(99)00070-X

Castro J, Manga M, Cashman K (2002) Dynamics of obsidian flows inferred from microstructures: insights from microlite preferred orientations. Earth Planet Sci Lett 199:211–226. https://doi.org/10.1016/S0012-821X(02)00559-9

Castro JM, Cashman KV, Manga M (2004) A technique for measuring 3D crystal-size distributions of prismatic microlites in obsidian. Am Miner 88(8–9):1230–1240

Clark J, Appleman D, Papike J (1969) Crystal-chemical characterization of clinopyroxenes based on eight new structure refinements. Miner Soc Am Spec Pap 2:31–50

Donnelly-Nolan JM, Champion DE, Grove TL (2016) Late Holocene volcanism at Medicine Lake volcano, northern California Cascades. US Geol Surv Prof Pap 1822:59

Fink JH (1983) Structure and emplacement of a rhyolitic obsidian flow: Little Glass Mountain, Medicine Lake Highland, northern California. GSA Bull 94(3):362–380

Fitzgerald JD, Parise JB, Mackinnon IDR (1986) Average structure of an An48 plagioclase from the Hogarth Ranges. Am Miner 71:1399–1408

Gardner JE, Llewellin EW, Watkins JM, Befus KS (2017) Formation of obsidian pyroclasts by sintering of ash particles in the volcanic conduit. Earth Planet Sci Lett 459:252–263. https://doi.org/10.1016/j.epsl.2016.11.037

Giachetti T, Gonnermann HM, Gardner JE, Shea T, Gouldstone A (2015) Discriminating secondary from magmatic water in rhyolitic matrix-glass of volcanic pyroclasts using thermogravimetric analysis. Geochim Cosmochim Acta 148:457–476. https://doi.org/10.1016/j.gca.2014.10.017

Giordano D, Russell JK, Dingwell DB (2008) Viscosity of magmatic liquids: a model. Earth Planet Sci Lett 271(1–4):123–134. https://doi.org/10.1016/j.epsl.2008.03.038

Gonnermann HM, Manga M (2003) Explosive volcanism may not be an inevitable consequence of magma fragmentation. Nature 426(6965):432–435

Gonnermann HM, Manga M (2005) Flow banding in obsidian: a record of evolving textural heterogeneity during magma deformation. Earth Planet Sci Lett 236:135–147. https://doi.org/10.1016/j.epsl.2005.04.031

Grove TL, Donnelly-Nolan JM, Housh T (1997) Magmatic processes that generated the rhyolite of Glass Mountain, Medicine Lake volcano, N. California. Contrib Miner Pet 127(3):205–223. https://doi.org/10.1007/s004100050276

Haerinck T, Wenk H-R, Debacker TN, Sintubin M (2015) Preferred mineral orientation of a chloritoid-bearing slate in relation to its magnetic fabric. J Struct Geol 71:125–135. https://doi.org/10.1016/j.jsg.2014.09.013

Hosemann R, Hindeleh AM, Brückner R (1991) Paracrystalline lattice structure of silica glass, α- and β-crystobalite. Phys Stat Sol A 126:313–324

Jeffery GB (1922) The motion of ellipsoidal particles immersed in a viscous fluid. Proc R Soc Lond Ser A 102:169–179

Kanitpanyacharoen W, Parkinson DY, de Carlo F, Marone F, Wenk H-R, MacDowell A, Mokso R, Stampanoni M (2013) A comparative study of X-ray microtomography on shales at different synchrotron facilities: ALS, APS and

SLS. J Synchrotron Radiat 20:1–9. https://doi.org/10.1107/S0909049512044354

Le Bail A (1995) Modelling the silica glass structure by the Rietveld method. J Non-Cryst Solids 183:39–42

Lutterotti L, Ceccato R, Dal Maschio R, Pagani E (1998) Quantitative analysis of silicate glass in ceramic materials by the Rietveld method. Mater Sci Forum 278–281:87–92

Lutterotti L, Vasin R, Wenk H-R (2014) Rietveld texture analysis from synchrotron diffraction images: I. Basic analysis. Powder Diffr 29:76–84. https://doi.org/10.1017/S0885715613001346

Manga M (1998) Orientation distribution of microlites in obsidian. J Volcanol Geotherm Res 86:107–115. https://doi.org/10.1016/S0377-0273(98)00084-5

Manga M (2005) Deformation of flow bands by bubbles and crystals. Geol Soc Am Spec Pap 396:47–53

Manley CR, Fink JH (1987) Internal textures on rhyolite flows as revealed by research drilling. Geology 15:549–552

March A (1932) Mathematische Theorie der Regelung nach der Korngestalt bei affiner Deformation. Z Kristallog 81:285–297

Matthies S, Wenk H-R (2009) Transformations for monoclinic crystal symmetry in texture analysis. J Appl Cryst 42:564–571. https://doi.org/10.1107/S0021889809018172

Miao J, Ercius P, Billinge SJL (2016) Atomic electron tomography: 3D structures without crystals. Science 353:1380. https://doi.org/10.1126/science.aaf2157

Midgley PA, Ward EPW, Hungria AB, Thomas JM (2007) Nanotomography in the chemical, biological and materials science. Chem Soc Rev 36:1477–1494. https://doi.org/10.1039/b701569k

Oertel G (1983) The relationship of strain and preferred orientation of phyllosilicate grains in rocks—a review. Tectonophysics 100:413–447

Oertel G (1985) Reorientation due to grain shape. In: Wenk HR (ed) Chapter 12 in preferred orientation in deformed metals and rocks: an introduction to modern texture analysis. Academic Press, Orlando, pp 259–265

Popa NC (1998) The hkl dependence of diffraction-line broadening caused by strain and size for all Laue groups in Rietveld refinement. J Appl Cryst 31:176–180

Rahnama M, Koch DL, Shaqfeh ES (1995) The effect of hydrodynamic interactions on the orientation distribution in a fiber suspension subject to simple shear flow. Phys Fluids 7(3):487–506

Rust AC, Manga M, Cashman KV (2003) Determining flow type, shear rate and shear stress in magmas from bubble shapes and orientations. J Volcanol Geoth Res 122(1–2):111–132. https://doi.org/10.1016/S0377-0273(02)00487-0

Sander B (1950) Einführung in die Gefügekunde der Geologischen Körper. Zweiter Teil: Die Korngefüge. Springer, Wien, pp 409

Smith JV (2002) Structural analysis of flow-related textures in lavas. Earth Sci Rev 57(3–4):279–297

Soda Y, Wenk H-R (2014) Antigorite crystallographic preferred orientations in serpentinites from Japan. Tectonophysics 615–616:199–212. https://doi.org/10.1016/j.tecto.2013.12.016

Stampanoni M, Mokso R, Marone F, Vila-Comamala J, Gorelick S, Trtik P, Jefimovs K, David C (2010) Phase-contrast tomography at the nanoscale using hard X rays. Phys Rev B 81(R):140105. https://doi.org/10.1103/PhysRevB.81.140105

Tatlock DB, Flanagan FJ, Bastron H, Berman S, Sutton AL Jr (1976) Rhyolite, RGM-1, from Glass Mountain, California. In: Flanagan FJ (ed) Descriptions and analyses of eight new USGS rock standards. USGS Professional Paper 840, pp 11–14

Tuffen H, Dingwell DB, Pinkerton H (2003) Repeated fracture and healing of silicic magma generate flow banding and earthquakes? Geology 31(12):1089–1092

Ventura G (2004) The strain path and kinematics of lava domes: an example from Lipari (Aeolian Islands, Southern Tyrrhenian Sea, Italy). J Geophys Res Solid Earth. https://doi.org/10.1029/2003JB002740

Voltolini M, Zandomeneghi D, Mancini L, Polacci M (2011) Texture analysis of volcanic rock samples: quantitative study of crystals and vesicles shape preferred orientation from X-ray microtomography data. J Volcanol Geotherm Res 202(1–2):83–95

Waters LE, Andrews BJ, Lange RA (2015) Rapid crystallization of plagioclase phenocrysts in silicic melts during fluid-saturated ascent: phase equilibrium and decompression experiments. J Petrol 56:981–1006. https://doi.org/10.1093/petrology/egv025

Wenk H-R, Matthies S, Donovan J, Chateigner D (1998) BEARTEX: a Windows-based program system for quantitative texture analysis. J Appl Crystallogr 31:262–269

Wenk H-R, Kanitpanyacharoen W, Voltolini M (2010) Preferred orientations of phyllosilicates: comparison of fault gouge shale and schist. J Struct Geol 32:478–481. https://doi.org/10.1016/j.jsg.2010.02.003

Wenk H-R, Lutterotti L, Kaercher P, Kanitpanyacharoen W, Miyagi L, Vasin RN (2014) Rietveld texture analysis from synchrotron diffraction images: II.

Complex multiphase materials and diamond anvil cell experiments. Powder Diffr 29:172–192. https://doi.org/10.1017/S0885715614000360

Wu L, Agnew SR, Ren Y, Brown DW, Clausen B, Stoica GM, Wenk H-R, Liaw PK (2010) The effects of texture and extension twinningon the low-cycle fatigue behavior of a rolled magnesium alloy, AZ31B. Mater Sci Eng A 527:7057–7067. https://doi.org/10.1016/j.msea.2010.07.047